Nanoscale electrical properties of cluster-assembled palladium oxide thin films

V. Cassina,[1,*] L. Gerosa,[2] A. Podestà,[1,†] G. Ferrari,[2] M. Sampietro,[2] F. Fiorentini,[1] T. Mazza,[1] C. Lenardi,[3] and P. Milani[1,‡]
[1]*Dipartimento di Fisica and C.I.Ma.I.Na., Università degli Studi di Milano, via Celoria 16, 20133 Milano, Italy*
[2]*Dipartimento di Elettronica ed Informazione, Politecnico di Milano, P.zza L. da Vinci 32, 20133 Milano, Italy*
[3]*C.I.Ma.I.Na. and Istituto di Fisiologia Generale e Chimica Biologica, Università degli Studi di Milano, via Trentacoste 2, 20134 Milano, Italy*

(Received 6 October 2008; revised manuscript received 30 January 2009; published 17 March 2009)

The electrical properties of cluster-assembled nanostructured palladium oxide (ns-PdO_x) thin films grown by supersonic cluster beam deposition have been characterized by means of a customized ac current-sensing atomic force microscope. Scanning impedance microscopy is shown to provide a deep picture of the electrical properties of thin nanostructured interfaces even in the case of very soft and poorly adherent films. In particular, the dielectric constant of ns-PdO_x can be quantitatively determined as well as its *I-V* characteristics. Moreover, the measurement of the tip-sample parasitic capacitance can be exploited to probe the overall mesoscale conductive character of thin films and to give a complementary and more precise view of the oxidation of ns-PdO_x obtained by x-ray photoemission spectroscopy.

DOI: 10.1103/PhysRevB.79.115422 PACS number(s): 81.07.−b, 73.50.−h, 07.79.Lh

I. INTRODUCTION

The integration of nanostructured (ns) thin films and nanoparticles in planar microfabrication processes for the production of micro-electro-mechanical systems (MEMS), microelectronic components, lab-on-a-chip devices, and sensors is the ground where the combination of top-down and bottom-up approaches can provide innovative solutions with high-technological and economic value.[1] The physicochemical properties and the high surface-to-volume ratio, typical of nanostructured materials resulting from the assembling of nanoparticles, make them particularly suitable to improve the performance of microdevices such as chemical sensors and biosensors, field-emission devices, and catalytic microreactors.[2]

Nanostructured metal-oxide films are a class of systems offering a wide range of technological opportunities,[3] among them, one of the most versatile is palladium oxide.[4] For example, supported PdO catalysts are used for low-temperature combustion of methane,[4] and the oxidation processes of palladium nanoparticles supported by metal-oxide surfaces have been investigated as a model system for catalysis.[5] However, the influence of oxide formation on the catalytic activity still remains a matter of discussion.[6] PdO, a *p*-type semiconductor thermally stable up to 800 °C with a relatively low work function (3.9 eV), is a suitable material for field-emission applications and as an electrode material in surface-conduction electron emitter displays.[7] Palladium oxide is also used as an active material in chemoresistive gas-sensing microdevices since gas exposure results in a change in its electrical conduction properties.[8,9]

Properties such as nanoscale morphology and structure, presence of defects, and local oxidation state are expected to influence the electrical response of interfaces to external stimuli. Although the concurrent investigation of morphological and electrical properties of nanostructured PdO films is crucial for their exploitation as active layers in gas sensors and catalytic systems, to date scarce data are available about their nanoscale electrical properties.

The atomic force microscope (AFM) (Ref. 10) is a well-established tool, enabling topographic imaging of surfaces with nanometer spatial resolution. In the last decade, ac and dc current-sensing AFMs equipped with conductive probes and dedicated electronics for the generation and acquisition of electrical signals were developed.[11–15] These instruments allowed one to characterize different electrical properties simultaneously to topography, such as conductivity[16–18] and capacitance.[19,20] An optimized low-noise transimpedance amplifier was recently developed[21] and integrated in a commercial AFM to characterize the capacitive properties of interfaces with attofarad resolution.[22] This system was successfully employed to characterize the dielectric and transport properties of micropatterned/nanopatterned surfaces[23] and biointerfaces.[24]

Here we present a study of the electrical properties of nanostructured palladium oxide films (hereafter ns-PdO_x) produced by supersonic cluster beam deposition.[25] The influence of different oxidation procedures on the electrical properties of ns-PdO_x films was characterized using a custom ac current-sensing AFM based on a low-noise transimpedance amplifier.[21] The use of this custom AFM allowed us to study very soft samples that require extremely low applied loads. We show that an optimized scanning impedance microscope permits an accurate characterization of the nanoscale and mesoscale electrical properties of ns-PdO_x films and it can unravel relevant aspects for the understanding of the oxidation processes in cluster-assembled films, providing complementary information to traditional surface science techniques, such as x-ray photoemission spectroscopy (XPS), which are limited by their low depth sensitivity.

II. EXPERIMENTAL SETUP

A. Deposition of cluster-assembled films

Ns-PdO_x films were grown on various substrates by depositing under high-vacuum conditions (10^{-6} Torr)—a supersonic beam of Pd clusters produced by a pulsed micro-

plasma cluster source (PMCS), as described in detail in Refs. 25 and 26. Briefly, a palladium target rod is placed in the PMCS ceramic cavity where a solenoid valve delivers pulses of He gas. A He plasma is ignited by a pulsed electric discharge between the Pd rod (cathode) and an anode, producing the ablation of the target. The ablated Pd atoms thermalize inside the cavity by collision with the inert gas condensing into clusters; the He-cluster mixture is then expanded in a vacuum chamber through a nozzle to form a supersonic beam. Typical cluster size distribution, as produced by the PMCS, is peaked in the range of several hundred atoms per cluster. The kinetic energy upon landing is on the order of 0.5 eV per atom, which is small enough to avoid cluster fragmentation.[2] The deposition takes place on substrates intercepting the supersonic beam in a second differentially pumped chamber separated from the expansion chamber by an electroformed skimmer at a deposition rate of about 1 nm/min. Cluster-assembled films were deposited on circular smooth glass substrates with diameter of 10–15 mm, on which Cu/Au microelectrodes with dimensions of 60 μm$\times$3 mm were evaporated. These microelectrodes are connected on a side to a long perpendicular 1.5-mm-wide Cu/Au strip for easier soldering and wiring. The microelectrodes are designed to minimize the stray capacitance between the substrate and the AFM probe in order to increase the resolution of the capacitance measurements.[27] The stray capacitance can be kept as low as $\sim$40 fF with this arrangement, which is much smaller than the $\sim$400–500 fF measured on an extended electrode obtained by depositing a thin gold film on a glass substrate. We adopted two different strategies to oxidize the Pd clusters: the introduction of a 80 at. % He and 20 at. % O_2 mixture as carrier gas into the cluster source during the ablation of the Pd target and post-deposition thermal treatments in air at 200 °C or 400 °C for 4 h of the Pd films produced with He as carrier gas. We have therefore characterized three types of ns-PdO_x films: the as-deposited films, produced using He [hereafter ns-PdO_x(He)] and the He-O_2 mixture [ns-PdO_x(He:O_2)] as carrier gas, and the films deposited with He that underwent thermal treatments [hereafter annealed ns-PdO_x(He)].

B. Custom ac current-sensing AFM

A block diagram of the experimental setup for the nanoscale electrical measurements is shown in Fig. 1. It consists in a commercial multimode nanoscope IV AFM (Veeco Instruments), a custom wide-bandwidth current amplifier, and a digital lock-in SR830 (Stanford Research System). A fast analog-digital acquisition board (PCI-6115, National Instruments) and a high-resolution analog-digital acquisition board (PCI-6251, National Instruments) are also available. The ac and dc driving voltages for capacitance and *I-V* measurements are provided by the lock-in and the high-resolution board, accordingly, and are applied between the AFM probe and the sample using a breakthrough box placed between the AFM and its controller. A current limiter in series with the tip limits the current to 150 nA in order to avoid damage at the tip coating in case of a highly conductive sample.

A key element of the setup is the fully customized current amplifier, specifically designed to combine high resolution

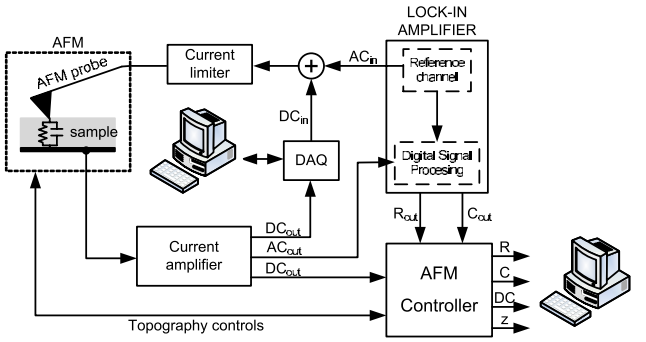

FIG. 1. (Color online) Block diagram of the implemented instrumentation for nanoscale impedance microscopy. A fully customized wide-bandwidth amplifier has been coupled to an atomic force microscope in a lock-in detection scheme to enable simultaneous dc and impedance measurement.

with wide bandwidth and described elsewhere.[21,22,27] Shortly, the amplifier is based on an integrator-differentiator scheme combined with an active feedback to collect continuously the dc input current. The system only has 4 fA/$\sqrt{\text{Hz}}$ noise up to a few kilohertz, a 1 MHz bandwidth, and ensures unlimited measuring time even with 10 nA dc input current. Both the ac and dc currents that flow through the sample are simultaneously measured by the current amplifier and converted to voltages. The ac signal is processed by the digital lock-in that measures the in-phase and in-quadrature components of the measured current and calculates the resistance and capacitance of the sample. The system can operate in both spectroscopy and imaging modes. In spectroscopy mode, *I-V* analysis can be performed using a software interface (LABVIEW) that drives the dc ramp signal and manages the current and voltage data acquisition. During acquisition of the *I-V* characteristics, the tip can be either kept fixed in one location or allowed to scan a finite profile length in one direction. Another spectroscopy mode consists in recording the value of the capacitance as a function of the tip-sample distance during approaching-retracting cycles. The in-plane tip position is kept fixed in this case. In imaging mode, a finite surface area is scanned by the biased AFM tip, while the dc output of the current amplifier is sent back into the controller and mapped together with the topography in order to characterize the dc conductivity of the sample. The output signals of the lock-in stage (R_{out} and C_{out}) can be also acquired in order to map the resistive and capacitive properties simultaneously to the topography.

The typical experimental procedure was to scan the surface of ns-PdO_x films in tapping mode in order to find good regions for the analysis than switching to contact mode and probe the conductivity of the sample in spectroscopy or imaging modes. The cantilever choice and the fine control of the applied force during the measurements turned out to be crucial because the hardness and adhesion of ns-PdO_x films are very poor. Tips coated with a hard film of W_2C mounted on soft cantilevers (force constant k=0.3 N/m) were used. Typical radii of curvature of these tips are in the range 50–200 nm. Keeping the microscope head in a dry nitrogen atmosphere prevented the formation of capillary necks between the probe and the surface, minimizing adhesion forces,

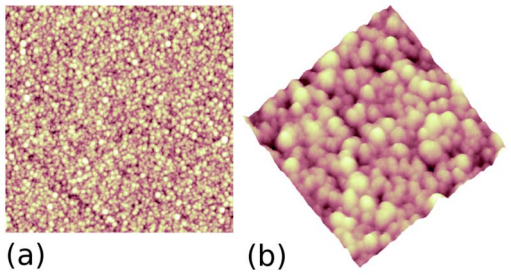

FIG. 2. (Color online) Atomic force microscopy topographic maps of a ns-PdO_x(He:O_2) film. (a) Top view, scan size: 2×2 μm^2, vertical scale: 10 nm, highest points are the brightest. (b) Three-dimensional view of a 500×500 nm^2 area, vertical scale: 10 nm.

while suspending the AFM on a heavy plate by means of elastic cords provided good insulation from vibrations.

III. RESULTS AND DISCUSSION

A. Morphology of ns-PdO_x films

Figure 2 shows topographic maps of a ns-PdO_x(He:O_2) film acquired by AFM. The morphology of as-deposited and annealed ns-PdO_x(He) films is similar to the one shown in Fig. 2. The typical morphology of ns-PdO_x films consists in a fine raster of nanometer-sized grains. Root-mean-square surface roughness of films with thickness in the range 10–20 nm is typically below 10 nm (2 nm in the case of the film shown in Fig. 2). The smallest among the visible grains (<5 nm) are primeval clusters produced in the source, while larger grains result from the aggregation and coalescence of smaller clusters. The real size of the smallest clusters is more than doubled by the limited resolution of the AFM, determined primarily by the finite tip radius (5–10 nm). Such granular nanoporous structure is a consequence of the low-energy deposition regime typical of supersonic cluster beam deposition,[2] in this regime the cluster-assembled film is very soft and it can be easily detached from the substrate. Because of this peculiar nanostructure, the electrical properties of ns-PdO_x films may vary on the nanometer scale, and therefore the electrical characterization device must possess a truly nanometer spatial resolution in order to faithfully reproduce the expected spatial variability of electrical properties.

B. Characterization of film oxidation by XPS and by measurement of the parasitic capacitance

The results of XPS analysis of samples produced with different deposition conditions and/or postdeposition treatments (data not shown) are very similar.[28] All spectra of nanostructured samples show indeed the same peaks with the same proportions: two peaks from surface palladium oxide and one from Pd metal, whose binding energies are in agreement with the literature.[29] In order to understand the similarity of XPS results, it must be considered that the XPS signal originates from a surface region of the film extending into the bulk to depths of the order of the escape distance of photoelectrons (1–3 nm at 350 eV), which is comparable with the cluster size. Therefore XPS cannot reveal any differences in the oxidation state of clusters lying in the deeper layers of the films, where the oxidation state of the different samples is likely to be more diverse. XPS, which is widely used as a surface characterization technique (especially for oxides), turns out to be not very useful in those systems where the size of the building blocks (the clusters) is comparable with the probing depth.

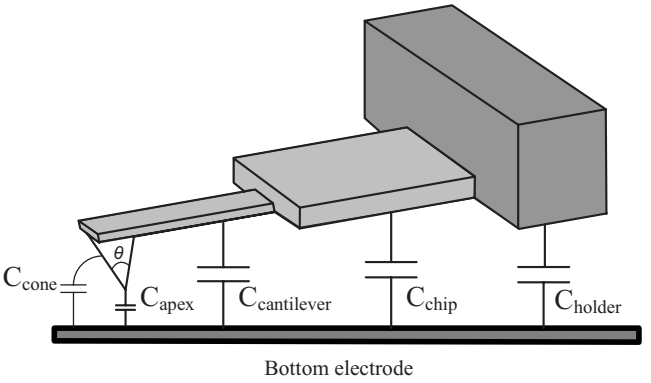

FIG. 3. A scheme of the contributions to the total tip-sample capacitance C; the tip apex capacitance C_{apex} is the true local capacitance, depending on the film properties, while the tip cone, the cantilever, the chip, and the tip holder determine the parasitic capacitance C_{par}.

In order to get a more detailed understanding of the oxidation mechanisms of thin ns-PdO_x films, it is necessary to use, in combination to a high surface-sensitive technique such as XPS, another technique that can provide information about the innermost film regions. To this purpose we observe that a direct measurement of the parasitic contribution to the total capacitance obtained by the current-sensing AFM allows one to differentiate different oxidation states of the films and, together with the XPS data, to build a clear picture of the oxidation paths of Pd nanoparticles and films produced using different deposition conditions and postdeposition treatments. It is worth noting that the parasitic contribution is an unwanted contribution to the total capacitance in impedance nanoscale measurements. As discussed in the experimental session, care must be taken in order to minimize this parasitic capacitance. Here we show that this unwanted effect can be exploited beneficially to probe the overall conductive character of a thin coating at the mesoscale. The capacitances associated to the different parts of the tip-cantilever assembly of an AFM are schematically represented in Fig. 3.

For tip-sample separations of several microns, the contribution of the tip apex C_{apex} is negligible and the measured capacitance is equal to the parasitic (or stray) capacitance $C_{par}=C_{cone}+C_{cantilever}+C_{chip}+C_{holder}$.[22,30,31] An insulating film between the AFM tip and the microelectrodes would act as a dielectric slab, providing a parasitic capacitance proportional to the area of the underlying microelectrodes. Conversely, a metallic film will act as a counterelectrode as large as the glass substrate, determining a much larger parasitic capacitance. A direct measurement of the parasitic capacitance at fixed tip-sample distance and overall tip-sample geometry on different films can be used therefore to investigate

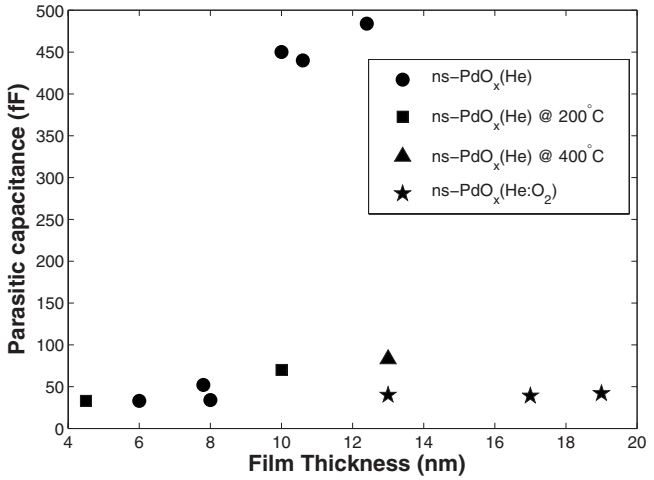

FIG. 4. Parasitic capacitance vs film thickness for as-deposited and annealed ns-PdO_x(He) and for ns-PdO_x(He:O_2) films.

the electric properties of ns-PdO_x films on a length scale larger than the tip apex.

In Fig. 4 we report the parasitic capacitances measured on different ns-PdO_x samples by placing the tip 20 μm far away from the sample surface and by applying an ac voltage to the tip. Ns-PdO_x(He:O_2) films (Fig. 4, stars) present the lowest parasitic capacitance (~35 fF), equal to that measured above the naked microelectrodes. The low parasitic capacitance suggests that ns-PdO_x(He:O_2) films are nonconductive. The largest values of the parasitic capacitance (up to ~500 fF) are measured on ns-PdO_x(He) films with thickness above 10 nm (Fig. 4, disks). Such a high parasitic capacitance is in agreement with the figure of an AFM probe coupled with a counter electrode (the uniform metalliclike Pd film) as large as the glass substrate. Figure 4 shows however more subtle effects. By decreasing the thickness of ns-PdO_x(He) films, a transition from metallic (capacitance ~500 fF) to insulator character (capacitance ~40 fF) is observed. We can qualitatively explain these results using the concept of percolation applied to electrical conductivity.[32,33] Palladium clusters produced in the absence of oxygen are metallic and only poorly oxidized upon exposure to air. If the thickness of the film is very low, the different regions of the film are not electrically interconnected. In the absence of a network of conductive paths connecting metallic domains, the AFM tip can establish a capacitive coupling only with the microelectrodes. As the film thickness increases, percolative paths begin to connect different regions of the film and the film as a whole to the microelectrodes. The effective area of the counterelectrode increases accordingly. When the film thickness is sufficiently high, the film behaves like an extended electrode, whose area is as large as the area of the glass substrate. The sudden transition from low to high parasitic capacitance observed for ns-PdO_x(He) films at thickness of ~10 nm suggests the existence of percolative phenomena. Macroscopic measurements of film conductance performed *in situ* during ns-Pd film growth confirm the existence of a percolation threshold for the electrical conductivity.[34] We exclude that the observed behavior can be determined by a z-dependent oxidation degree of the films. Because of their reduced thickness (below 20 nm), and being the typical cluster size of the order of 1 nm, ns-PdO_x(He) films are likely uniformly (and poorly) oxidized across their whole thickness upon exposure to ambient oxygen. Moreover, the oxidation of the nanoparticles induced by ambient oxygen is very superficial and cannot interrupt the conductive paths formed by metallic clusters during deposition in ultrahigh vacuum.

Annealed ns-PdO_x(He) films with thickness above 10 nm possess intermediate parasitic capacitances between those of ns-PdO_x(He) and ns-PdO_x(He:O_2) films, as observed in Fig. 4—squares and triangles. This can be interpreted in terms of a reduction in the effective area of the metallic counterelectrode due to partial oxidation of the ns-PdO_x(He) film. Upon annealing up to 400 °C, the outer surface of Pd clusters gets further oxidized. Although oxidation is more effective at the film surface, it takes place also in the bulk, thanks to the nanoporosity of the films. Pd clusters are partially coalesced in the film. Upon annealing, surface clusters are likely to be completely oxidized on their surface, and therefore become electrically disconnected. Bulk Pd clusters however are only partially oxidized, thus remaining electrically connected. The larger the film thickness, the larger is the probability that metallic connected paths survive to oxidation upon annealing in the bulk of the film. This is consistent with the observation that thicker annealed ns-PdO_x(He) films show larger capacitances.

The parasitic capacitance data suggest a simple picture of the oxidation mechanisms of Pd clusters. The fact that the parasitic capacitance of ns-PdO_x(He:O_2) films is always at its minimum, irrespective to film thickness, supports the hypothesis that the injection of oxygen in the cluster source induces the formation of an outer oxide shells in all metallic Pd clusters. When deposited onto a substrate, Pd/PdO_x core-shell nanoparticles cannot form a conductive film, even well above the percolation threshold, because the oxide layer prevents the metallic cores from getting in contact. In turn, Pd clusters produced when only He is present into the source are bulky metallic, and get only poorly oxidized at their surface upon exposure to ambient oxygen. When deposited onto the substrate they form electrically connected nanodomains. These domains, when the ns-PdO_x(He) film thickness is above the percolation threshold, become connected on a macroscopic scale, giving it an overall metallic character. Annealing makes the very first surface layers of ns-PdO_x(He) films similar to those of ns-PdO_x(He:O_2) films and significantly reduce the fraction of electrically connected Pd metal in the innermost film layers, though it does not completely destroy the overall conductive character of the bulk film.

Despite the striking difference in the parasitic capacitance, the binding-energy spectra of ns-PdO_x(He) and ns-PdO_x(He:O_2) films are indeed at all similar; according to XPS data, both films seem to contain the same relative amount of oxidized and metallic palladium atoms. We have noticed however that only an interfacial layer of ns-PdO_x with thickness of the order of the photoelectron escape length (which is comparable to the cluster size) contributes to the XPS signal. This layer is actually similar in both as-deposited and annealed ns-PdO_x(He) and ns-PdO_x(He:O_2) films; this fact accounts for the similarity of XPS spectra.

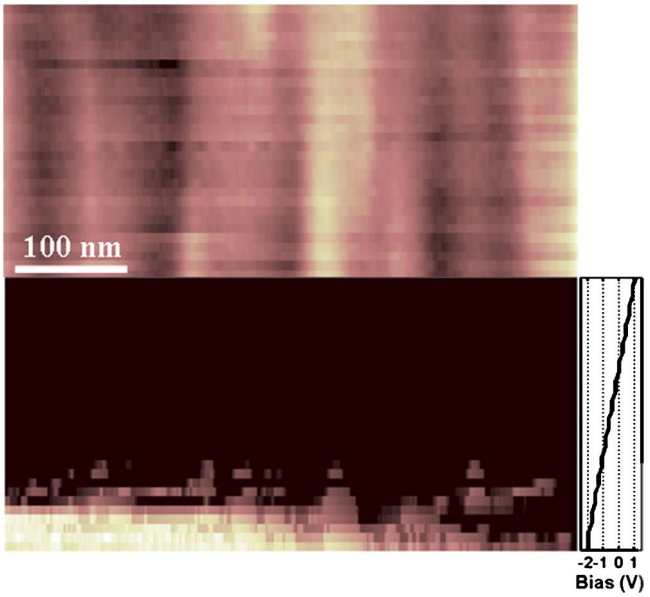

FIG. 5. (Color online) Representative topographic and current maps acquired on a ns-PdO_x(He) film. A finite scan size of 500 nm was allowed in the fast-scan direction, while the slow-scan direction was disabled. The bias applied to the AFM tip during the scan is shown in the side box.

The difference between the films manifests at depths exceeding the photoelectron escape length; in ns-PdO_x(He) films clusters are mostly metallic, while in ns-PdO_x($He:O_2$) films they are at all similar to surface clusters—a metallic core surrounded by an oxide shell. Parasitic capacitance measurements are sensitive to the surface as well as to the bulk layers of the films and can discriminate between the two cases.

C. *I-V* analysis of ns-PdO_x films

The electrical conductivity of ns-PdO_x films has been quantitatively investigated by measuring the local current-versus-voltage characteristics (*I-V* curves). To this purpose, the AFM tip was kept in contact with the film surface with a mild applied load below 10 nN and the dc current measured while the bias was ramped. We allowed for a finite scan size during the acquisition of the *I-V* curve in order to investigate different locations and map local inhomogeneities. This is also a convenient way of ensuring on the average a better electrical contact and smearing out possible topographic contributions to the *I-V* curve. The tip was scanned along the same line. Scan size was set to 500 nm and scanning velocity was set below 100 nm/s. Each applied bias was kept constant along several scan lines to ensure a good statistics. Figure 5 shows a representative pair of topographic and current maps acquired simultaneously on a ns-PdO_x(He), as described above. The bias applied to the AFM tip was ramped from positive to negative values with respect to the sample. The bias applied during each scan line is shown in the side box of Fig. 5. The same topographic profile is repeated in the topographic map of Fig. 5. The fact that the profile does not change significantly during the scan suggests that we can exclude destructive interactions between the AFM tip and the film, which is a necessary condition for performing any electrical characterization in contact mode. The current map shows no signal until a negative bias of approximately −1.5 V is applied; after that moment, the current map shows nanoscale variations.

Figure 6(a) shows a complete *I-V* dispersion measured on a ns-PdO_x(He) film above the gold microelectrode. This sample with unknown thickness showed a low parasitic capacitance (C_{par}=25 fF). According to the results of Sec. III B, we can infer that the thickness of this film is below 10 nm. In Fig. 6(a) the current values measured for each applied voltage are spread over a large interval and the marker size in the figure does not allow one to appreciate their actual distribution, which looks deceptively uniform. In order to highlight the leading trends in the dispersion shown in Fig. 6(a), we binned the current axis and calculated average current values for each bin, in correspondence of each applied voltage. Typically, the obtained current histograms showed two distinct main contributions, as shown in the inset of Fig. 6(a). These contributions were fitted with Gaussian curves, in order to extract average values with their error (the standard deviations) and separate the different *I-V* trends. The results of this data analysis procedure for ns-PdO_x(He) are shown in Fig. 6(b). Two trends have been identified: one is flat and corresponds to the nonconducting nanoscale regions and the other is nonlinear and shows a diodelike behavior. The *I-V* analysis confirmed that this ns-PdO_x(He) film is not homogeneously conducting on the nanometer scale. Although the film is below the percolation threshold, a few conductive paths exist, which connect the film surface to the gold electrode some 10 nm below it. The presence of the two trends in the *I-V* dispersion reflects the peculiar nanoscale electrical inhomogeneity of cluster-assembled nanostructured films. In particular, ns-PdO_x(He) possesses a partially oxidized granular structure.

Figures 6(c) and 6(d) show the *I-V* curves of two other samples: a 10-nm-thick ns-PdO_x(He) film annealed at 200 °C for 4 h (C_{par}=70 fF) and an 11-nm-thick ns-PdO_x(He) film annealed at 400 °C for 4 h (C_{par}=83 fF). We have applied negative bias to the tip in order to avoid its oxidation and maximize the lifetime of the conductive tip. In all the curves it is possible to recognize threshold values of the applied voltage at which the current significantly rises above the zero level. For the as-deposited ns-PdO_x(He) film, the threshold value is ±0.8 V for both positive and negative applied voltages. In the sample annealed at 200 °C the threshold bias is shifted (in magnitude) to a larger value (~2 V). The maximum current intensity measurable is set by the current limiter (~150 nA). In the sample annealed at 400 °C the threshold bias values are further shifted toward larger absolute values (~3.4 V), after which the increase in current values is slower than in the previous curves. In this sample the current value reaches only −5 nA with an applied bias of −5 V. Our data support the hypothesis that annealing improves the film oxidation, especially in the topmost surface layers, which produces a decrease in electrical conductivity. The bulk cluster layers are less affected by the oxidation from ambient oxygen, therefore in both samples a conductive network survives to oxidation, determining a similar parasitic capacitance.

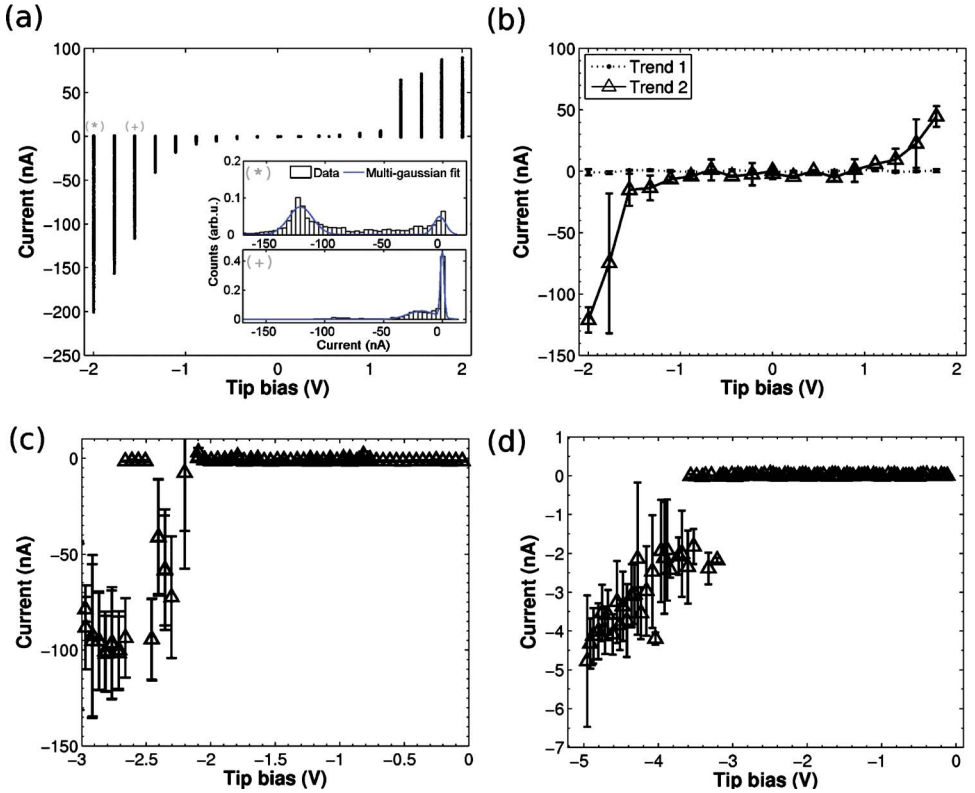

FIG. 6. (Color online) *I-V* curves acquired in spectroscopy mode on ns-PdO_x films. A scan size of 500 nm was allowed during acquisition of *I-V* curves, while the slow-scan direction was disabled. (a) Scattered *I-V* curve acquired on a ns-PdO_x(He) film. The inset shows the histograms of the current values measured for two applied bias and the multi-Gaussian fit. (b) The data shown in (a) after binning and multi-Gaussian fit for the identification of the leading trends; (c) *I-V* curve acquired on ns-PdO_x(He) annealed at 200 °C for 4 h; (d) *I-V* curve acquired on ns-PdO_x(He) annealed at 400 °C for 4 h.

D. Measurement of the dielectric constant of ns-PdO_x films

When the tip is far away from the electrode, the capacitance is determined primarily by the tip cone, the cantilever, the chip, and the tip holder. This parasitic contribution C_{par} to the total capacitance is approximately linear in the tip-electrode distance for variations in several hundred nanometers,[23]

$$C_{\mathrm{par}}(z) = q - mz, \tag{1}$$

where z is the tip-electrode separation, and m and q depend primarily on the geometry and size of the tip-electrode assembly. The apex contribution to the total capacitance is nonlinear and dominates at small separation. An approximate expression for C_{apex} in the presence of a dielectric film is[35]

$$C_{\mathrm{apex}}(z) = 2\pi\varepsilon_0 R \ln\left(1 + \frac{R(1-\sin\vartheta_0)}{z - h_0 + h_0/\varepsilon_r}\right) + K(R,\vartheta_0), \tag{2}$$

where h_0 is the film thickness, $z-h_0$ is the tip-film distance, ε_0 is the vacuum dielectric constant, ε_r is the relative dielectric constant of the film, R is the tip radius of curvature, ϑ_0 is the tip cone angle, and $K(R,\vartheta_0)$ is a constant. An approximate expression for the total capacitance $C(z)=C_{\mathrm{par}}(z)+C_{\mathrm{apex}}(z)$ is therefore

$$C(z) = q' - mz + 2\pi\varepsilon_0 R \ln\left(1 + \frac{R(1-\sin\vartheta_0)}{z - h_0 + h_0/\varepsilon_r}\right), \tag{3}$$

where $q'=q+K\approx q$, because $q \gg K$ (in our case, q is typically 3 orders of magnitude larger than K). The dependence of C_{apex} on ε_r suggests that the local relative dielectric constant of a thin slab of material can be inferred from the measured capacitance vs distance curves.

Figure 7 shows $C(z)$ vs z measured on a 17-nm-thick ns-PdO_x($He:O_2$) film. An offset of 47.69 fF has been subtracted from the curve. The capacitance and the cantilever deflection have been simultaneously recorded as a function of the distance traveled by the z piezo during approaching-retracting cycles. We obtained the correct tip-sample distance axis as the sum of the translated piezo traveled distance and the cantilever deflection[36] (the piezo traveled distance is

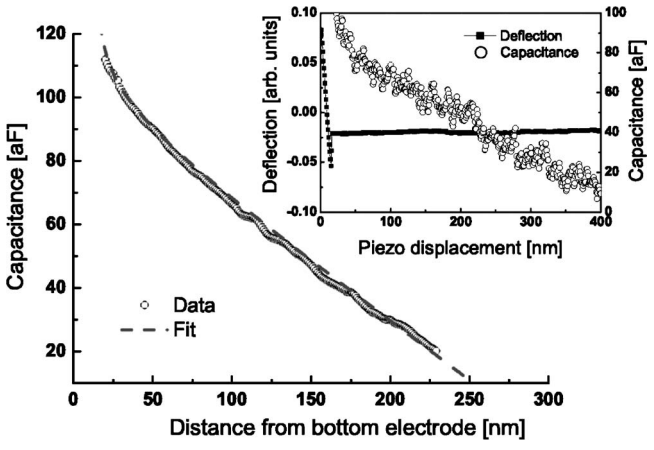

FIG. 7. Capacitance vs distance curve acquired on a ns-PdO_x($He:O_2$) film with thickness of 17 nm (a vertical offset of 47.6 fF has been subtracted). A sudden increase in the curve slope is detected at distances below ~60 nm. The dotted line is the fitting curve by Eq. (3). In the inbox the deflection of the cantilever and the simultaneously measured capacitance as a function of the distance traveled by the z piezo is shown. ac bias amplitude: 0.5 V; frequency: 100 kHz; dc bias: 0 V; integration time: 300 ms; approaching velocity: ~5 nm/s.

translated so that its value is zero in correspondence of the *jump-in* position, where the tip comes into contact with the film; the cantilever deflection is translated so that its value is zero at large distances). The film thickness was summed to the distance axis in order to obtain the distance from the bottom electrode. The subattofarad resolution was achieved by averaging ten curves acquired by applying an ac bias with amplitude of 500 mV and frequency of 100 kHz, and setting the integration time of the lock in to 300 ms and the approaching velocity to a few nm/s. The curve clearly shows a constantly sloped region at distances larger than 60 nm and a sudden increase in slope below 60 nm due to the apex contribution. The film thickness and the effective radius of curvature of the tip have been independently measured. An effective radius of curvature of the tip of $R=154\pm19$ nm has been obtained by fitting the capacitance-distance curve acquired on a bare metallic electrode using Eq. (3) with $h_0=0$. The film thickness has been calculated by imaging with the AFM a region of the film where a sharp step has been produced by partially masking the substrate during the deposition. Using the measured h_0 and R values in Eq. (3), the fit of the capacitance-distance curve acquired on the ns-PdO_x($He:O_2$) film provided $m\sim0.340\pm0.002$ aF/nm, $q=47.69\pm0.01$ fF, and an effective dielectric constant $\varepsilon_r=8.4\pm2.1$. We notice that the sensitivity of the parasitic capacitance to variations in heights is quite low, only 0.34 aF gained per nanometer. This is the result of the optimization of the geometry of the electrodes. In addition, we engaged the AFM tip in correspondence of the very end of the microcontacts in order to minimize all parasitic capacitive couplings between the cantilever assembly and the microelectrodes, keeping the cantilever from shadowing the electrodes.

We have reported a direct measurement of the dielectric constant of a nanostructured PdO_x film and one of the very few on PdO_x.[37] The measured value represents an effective dielectric constant averaged over an area of order $\sim\pi R^2=250\times250$ nm^2. The characterization of the local dielectric constant could be implemented in a force-volume-like scheme, where capacitance-distance curves are acquired at each point of a grid, spanning a finite area of the film surface, and postprocessing (fitting) of this capacitance-volume map would transform it in a map of the local dielectric constant, in one-to-one correspondence with the topographic map.

IV. CONCLUSIONS

We have performed an electrical characterization of nanostructured cluster-assembled palladium oxide films by means of a custom scanning impedance microscope based on a low-noise transimpedance amplifier integrated in a commercial AFM. Performing electric impedance rather than dc current measurements turned out to be a successful approach for the characterization of the electrical properties of very soft and poorly adherent samples with nanometer spatial resolution. Capacitance-distance spectroscopy proved to be a powerful tool to characterize the dielectric properties of nanostructured thin coatings in a noninvasive way; we measured the local dielectric constant of ns-PdO_x, which is $\varepsilon_r=8.4\pm2.1$. Local *I-V* spectroscopy revealed nanoscale electrical inhomogeneities in ns-PdO_x films, related to the peculiar nanostructured nature of these films and to the different deposition and postdeposition synthesis conditions. Moreover, we have shown that the direct measurement of the parasitic contribution to the total tip-sample capacitance, typically an unwanted side effect of nanoscale impedance measurement devices, can be beneficially exploited to probe the overall mesoscale conductive character of thin coatings. In particular, coupling parasitic capacitance measurements to XPS, we obtained a qualitative picture of the oxidation of Pd nanoparticles and thin nanostructured films under various conditions. The presence of oxygen in the cluster source turned out to enhance the formation of an oxide outer shell on metallic Pd clusters, allowing the deposition of insulating films. In turn, annealing in ambient atmosphere up to 400 °C of films assembled using Pd metallic clusters was effective in oxidizing a surface layer only a few nanometers thick while preserving the overall conductivity of the bulk film. These findings are interesting in view of the synthesis of nanostructured Pd films with controlled oxidation for applications as model catalytic surfaces or in biosensing and chemosensing devices.

ACKNOWLEDGMENTS

The authors would like to thank E. Barborini and L. Ravagnan for discussions. This research has been supported by the grant FISR 2004, "Matrici di microcombustori a idrogeno," and by Fondazione Cariplo under grant "Un approccio combinatorio a materiali nanostrutturati avanzati per l'optoelettronica, i microsensori e la catalisi."

*Present address: Dipartimento di Medicina Sperimentale, Università di Milano-Bicocca, Via Cadore 48, 20052 Monza (Milano), Italy.
†Corresponding author. alessandro.podesta@unimi.it
‡paolo.milani@mi.infn.it

[1] F. N. Institute, Productive Nanosystems: A Technology Roadmap, 2007, http://www.foresight.org
[2] K. Wegner, P. Piseri, H. V. Tafreshi, and P. Milani, J. Phys. D **39**, R439 (2006).
[3] G. Eranna, B. C. Joshi, D. P. Runthala, and R. P. Gupta, Crit. Rev. Solid State Mater. Sci. **29**, 111 (2004).
[4] T. Takeguchi, O. Takeoh, S. Aoyama, J. Ueda, R. Kikuchi, and K. Eguchi, Appl. Catal., A **252**, 205 (2003).
[5] G. Rupprechter and C. Weilach, J. Phys.: Condens. Matter **20**, 184019 (2008).
[6] T. Schalow, B. Brandt, M. Laurin, S. Schauermann, S. Guimond, H. Kuhlenbeck, J. Libuda, and H.-J. Freund, Surf. Sci. **600**, 2528 (2006).
[7] K. Yamamoto, T. Oguchi, K. Sasaki, I. Nomura, S. Uzawa, and K. Hatanaka, J. Soc. Inf. Disp. **14**, 73 (2006).

[8] F. Volkening, M. Naidoo, G. Candela, R. Holtz, and V. Provenzano, Nanostruct. Mater. **5**, 373 (1995).
[9] M. K. Kumar, M. R. Rao, and S. Ramaprabhu, J. Phys. D **39**, 2791 (2006).
[10] G. Binnig, C. F. Quate, and C. Gerber, Phys. Rev. Lett. **56**, 930 (1986).
[11] D. Lee, J. Pelz, and B. Bhushan, Rev. Sci. Instrum. **73**, 3525 (2002).
[12] R. Shao, S. Kalinin, and D. Bonnell, Appl. Phys. Lett. **82**, 1869 (2003).
[13] F. Houzé, P. Chretien, O. Schneegans, R. Meyer, and L. Boyer, Appl. Phys. Lett. **86**, 123103 (2005).
[14] L. Pingree and M. Hersam, Appl. Phys. Lett. **86**, 073509 (2005).
[15] L. Fumagalli, I. Casuso, G. Ferrari, and G. Gomila, in *Applied Scanning Probe Methods*, edited by B. Bhushan, H. Fuchs, and M. Tomitori (Springer, New York, 2008), Vol. 8.
[16] S. O'Shea, R. Atta, M. Murrell, and M. Wellland, J. Vac. Sci. Technol. B **13**, 1945 (1995).
[17] P. De Wolf, R. Stephenson, T. Trenkler, T. Clarysse, T. Hantschel, and W. Vandervorst, J. Vac. Sci. Technol. B **18**, 361 (2000).
[18] M. Porti, M. Nafria, X. Aymeruch, A. Olbrich, and B. Ebersberger, Appl. Phys. Lett. **78**, 4181 (2001).
[19] R. Barrett and J. Blanc, J. Appl. Phys. **70**, 2725 (1991).
[20] C. Williams, Annu. Rev. Mater. Sci. **29**, 471 (1999).
[21] G. Ferrari and M. Sampietro, Rev. Sci. Instrum. **78**, 094703 (2007).
[22] L. Fumagalli, G. Ferrari, M. Sampietro, I. Casuso, E. Martinez, J. Samitier, and G. Gomila, Nanotechnology **17**, 4581 (2006).
[23] L. Fumagalli, G. Ferrari, M. Sampietro, and G. Gomila, Appl. Phys. Lett. **91**, 243110 (2007).
[24] I. Casuso, L. Fumagalli, J. Samitier, E. Padros, L. Reggiani, V. Akimov, and G. Gomila, Nanotechnology **18**, 465503 (2007).
[25] H. V. Tafreshi, P. Piseri, G. Benedek, and P. Milani, J. Nanosci. Nanotechnol. **6**, 1140 (2006).
[26] E. Barborini, P. Piseri, and P. Milani, J. Phys. D **32**, L105 (1999).
[27] V. Cassina, Ph.D. thesis, Università degli Studi di Milano, 2007.
[28] The XPS characterization was performed at the ESCA microscopy beamline at the ELETTRA synchrotron-radiation source in Trieste, Italy (Ref. 38). The specimens were mounted on a heating stage and the temperature was monitored with a chromel-alumel thermocouple. The elemental edges and the valence-band spectra were acquired with pass energy of the analyzer set at 20 eV and kinetic-energy step of 0.04 eV. A reference spectrum of a metallic specimen was acquired on a Pd wire. The Pd wire was heated in vacuum up to 800 °C until the signal at the O 1*s* edge disappeared. The line shape of the peaks was assumed to be a linear combination of a Gaussian and a Lorentzian profile. The position, the intensity, and the FWHM of the peaks were allowed to vary during the fit procedure within reliable ranges. A Shirley-type background was assumed for fitting the intensity on the low- and high-energy sides of the energy interval. After background subtraction the spectra were normalized to the total area.
[29] D. Zemlyanov *et al.*, Surf. Sci. **600**, 983 (2006).
[30] D. Charrier, M. Kemerink, B. Smalbrugge, T. de Vries, and R. Janssen, ACS Nano **2**, 622 (2008).
[31] B. M. Law and F. Rieutord, Phys. Rev. B **66**, 035402 (2002).
[32] D. Stauffer, *Introduction to Percolation Theory* (Taylor & Francis, London, 1992).
[33] S. Yamamuro, K. Sumiyama, T. Hihara, and K. Suzuki, J. Phys.: Condens. Matter **11**, 3247 (1999).
[34] L. Ravagnan, G. Divitini, S. Rebasti, M. Marelli, P. Piseri, and P. Milani, arXiv:0902.0228 (unpublished).
[35] G. Gomila, J. Toset, and L. Fumagalli, J. Appl. Phys. **104**, 024315 (2008).
[36] H.-J. Butt, B. Cappella, and M. Kappl, Surf. Sci. Rep. **59**, 1 (2005).
[37] P. O. Nilsson and M. Shivaraman, J. Phys. C **12**, 1423 (1979).
[38] M. Marsi, L. Casalis, L. Gregoratti, S. Gunther, A. Kolmakov, J. Kovac, D. Lonza, and M. Kiskinova, J. Electron Spectrosc. Relat. Phenom. **84**, 73 (1997).